ADVANCED MATERIALS
www.advmat.de

Tailoring Single-Mode Random Lasing of Tin Halide Perovskites Integrated in a Vertical Cavity

Hamid Pashaei Adl, Jesús Sánchez-Díaz, Giovanni Vescio, Albert Cirera, Blas Garrido, Felipe Andres Vinocour Pacheco, Wiktor Żuraw, Łukasz Przypis, Senol Öz, Iván Mora-Seró, Juan P. Martínez-Pastor,* and Isaac Suárez**

The development of random lasing (RL) with predictable and controlled properties is an important step to make these cheap optical sources stable and reliable. However, the design of tailored RL characteristics (emission energy, threshold, number of modes) is only obtained with complex photonic structures, while the simplest optical configurations able to tune the RL are still a challenge. This work demonstrates the tuning of the RL characteristics in spin-coated and inkjet-printed tin-based perovskites integrated into a vertical cavity with low quality factor. When the cavity mode is resonant with the photoluminescence (PL) peak energy, standard vertical lasing is observed. More importantly, single mode RL operation with the lowest threshold and a quality factor as high as 1 000 (twenty times the quality factor of the resonator) is obtained if the cavity mode lies above the PL peak energy due to higher gain. These results can have important technological implications toward the development of low-cost RL sources without chaotic behavior.

1. Introduction

Random lasing (RL) appears when the optical feedback is generated by multiple scattering loops surrounding or embedding the gain medium.[1,2] Since scatters are either inherent of a polycrystalline material or can be introduced by relatively simple methods (nanoparticles, for example), the topic of RL has become very popular in the scientific community during the last years.[3] Nevertheless, the choice of uncontrolled scatters to provide the optical feedback also prevents the tuning of the emission characteristics, and usually results in instabilities on frequency, intensity, and shape of lasing spectra, usually composed of several lines.[4] To avoid such a chaotic behavior, the state of the art in RL has nowadays derived toward the investigation of suitable mechanisms to trap emitted photons in reduced areas and control the number of scattering modes able to lase. At these conditions, the system can become stable, and the emission characteristics (frequency, intensity, number of lasing modes and modal size) can be fully or partially predicted. Examples include shaping externally the pump pattern,[5,6] changing the temperature,[7,8] applying a mechanical stress,[9,10] or introducing plasmonic nanostructures.[11,12] All

H. P. Adl, J. P. Martínez-Pastor, I. Suárez
UMDO+, Instituto de Ciencia de los Materiales
University of Valencia
Valencia 46980, Spain
E-mail: juan.mtnez.pastor@uv.es

J. Sánchez-Díaz, I. Mora-Seró
Institute of Advanced Materials (INAM)
Jaume I University
Castelló de la Plana 12006, Spain
E-mail: sero@uji.es

G. Vescio, A. Cirera, B. Garrido
MIND-IN2UB, Department of Electronics and Biomedical Engineering
University of Barcelona
Martí i Franquès 1, Barcelona 08028, Spain

The ORCID identification number(s) for the author(s) of this article can be found under https://doi.org/10.1002/adma.202313252

DOI: 10.1002/adma.202313252

F. A. V. Pacheco, W. Żuraw, Ł. Przypis
Saule Research Institute
Dunska 11, Wroclaw 54-427, Poland

W. Żuraw, Ł. Przypis
Department of Semiconductor Materials Engineering
Wroclaw University of Science and Technology
Wybrzeze Wyspianskiego 27, Wroclaw 50-370, Poland

S. Öz
Saule S.A
Dunska 11, Wroclaw 54-427, Poland

S. Öz
Solaveni GmbH
Siemensstraße 42, 59199 Bönen, Germany

I. Suárez
Escuela Técnica Superior de Ingeniería
University of Valencia
Valencia 46100, Spain
E-mail: isaac.suarez@uv.es

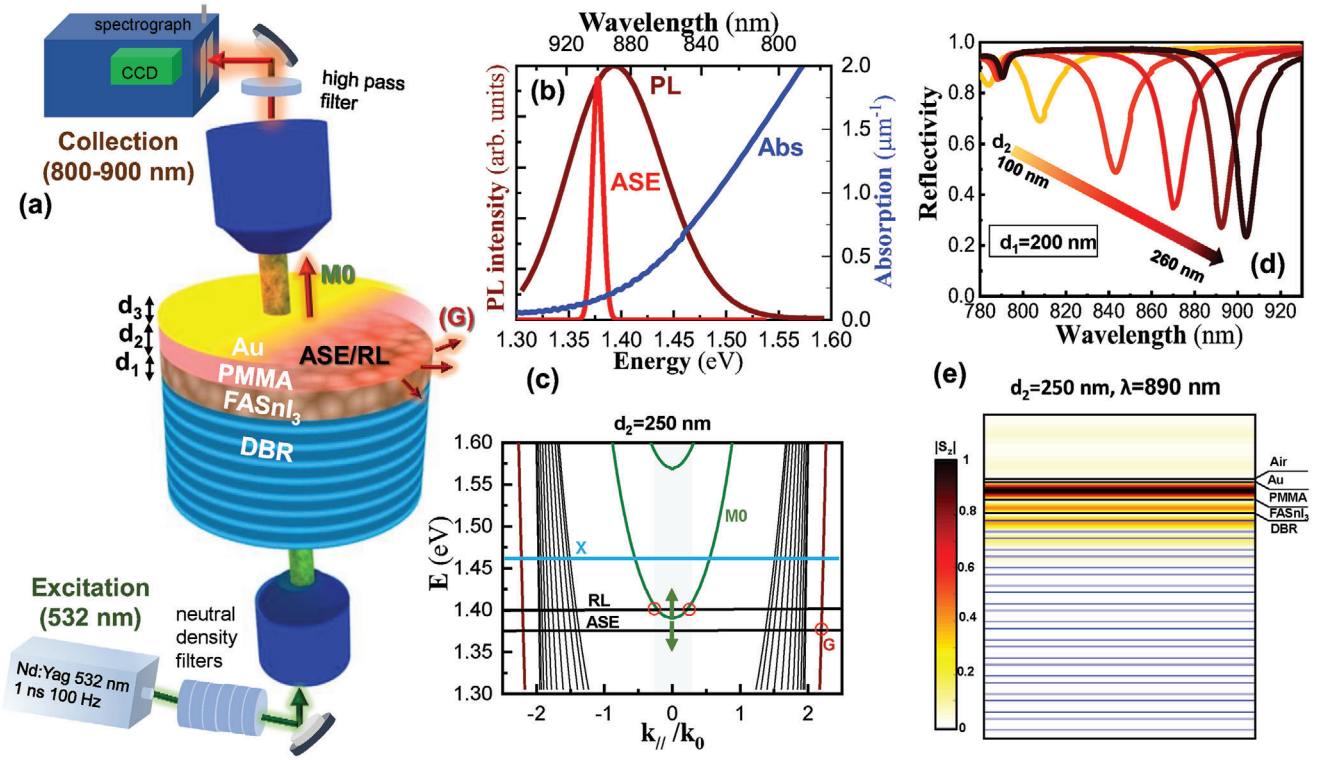

Figure 1. a) Vertical cavity laser structure and experimental configuration. b) Absorption (blue), PL (brown) and ASE band (red) of the $FASnI_3$ films used in this work. c) Dispersion diagram with $d_2 = 250$ nm. M0 (green) and G (brown) refers to the cavity and guided modes, respectively. Solid lines indicate the spectral position of the exciton resonance (X), ASE and RL. Gray area shows the numerical aperture collected by the objective. d) Reflectivity of the cavity ranging the PMMA thickness (d_2). (e) Simulation of the mode at 890 nm with $d_2 = 250$ nm.

these methods can be easily implemented on a broad range of low-cost materials, but only provide a partial control of the emission and/or require a post-fabrication tuning. A more sophisticated strategy consists of integrating the RL in an optical architecture. For instance, the coupling of the RL emission with the resonant mode of a planar cavity[13–15] represents a suitable way to provide directionality and an efficient extraction mechanism. Moreover, the optical architecture can provide a top-down design of the RL parameters. Here, photonic crystal membranes have been proposed as a patterned structural disorder where the emitted photons can be extremely localized under an Anderson-type regime.[16] Indeed, the dependence of the allowed photonic modes on the geometrical parameters of the membrane introduces the required degree of freedom to tune the RL characteristics, resulting in isolated single mode lines with remarkable stability.[17] On the other hand, the development of photonic crystals is challenging in both design and fabrication, needs a complex infrastructure, and the production is usually carried out on expensive III-V epitaxial semiconductors by complicated and non-scalable processes. Since one of the main advantages of a random laser is its simplicity and low-cost implementation, it is desirable to demonstrate a scalable platform for the full control of RL.

In this work, we demonstrate that simple vertical microcavities with low quality factor (Q-factor) provide an easy strategy to control the RL characteristics of polycrystalline thin films made by 3D and 2D/3D $FASnI_3$ (FA, formamidinium) – like perovskites. In analogy to the Pb-containing perovskites widely studied in the last years,[18,19] Sn halide perovskites are also direct band-gap semiconductors, but they are more environment friendly, which is of crucial importance for future sustainable optoelectronic technologies.[20] Among the most outstanding results, $FASnI_3$ has exhibited long radiative lifetimes,[21] efficient generation of amplified spontaneous emission (ASE),[22] as well as the required technological methods to obtain films with improved stability.[23] In this context, we have recently demonstrated that $FASnI_3$ films present superior features to generate unprecedent spectrally reproducible and narrow RL lines,[24] as well as optical waveguides able to extremely reduce the ASE threshold and provide directionality for the lasing lines.[25] The vertical cavity with low Q-factor chosen in this work represents the most suitable platform to obtain RL with relatively low threshold (10–50 μJ cm^{-2}) and lasing Q-factors higher than 1 000. Single mode operation is possible by appropriately tuning the energy position of the cavity resonant mode. The low Q-factor of the cavity not only reduces the cost and complexity of the device, but also helps to avoid strong excitonic coupling and favors tailoring between standard vertical lasing and efficiently outcoupled RL also in the vertical direction. Moreover, capping the $FASnI_3$ with the top Au mirror resulted in a reasonably good encapsulation for the tin perovskite, preventing oxidation under ambient conditions and allowing stable operation during > 8 h without the need of a vacuum chamber and/or additional encapsulation. These results can lead to important implications in the RL community and the development of

cheap RL sources for applications in communications, sensing, or displays.

2. Design and Simulations

The optical cavity used in this work consisted of a commercial distributed Bragg reflector (DBR) sequentially covered by $FASnI_3$, polymethyl methacrylate (PMMA) and Au, as illustrated in **Figure 1a** and described in the experimental methods. The device was analyzed in transmittance geometry by focusing the pump beam at 532 nm (1 ns, 100 Hz-20 kHz) from the back DBR mirror and collecting photoluminescence (PL) from the top Au side, as a function of the excitation fluence, as illustrated in Figure 1a. The target of the experiment is to couple the ASE/RL light generated in the semiconductor to the resonant mode of the cavity (M0) and to study how the spectral position of the mode controls the emission properties (spectral position, number of RL modes and threshold) of the device. As we recently demonstrated, the $FASnI_3$ thin films excited under nanosecond pulses give rise to an efficient generation of stimulated emission, with the propagation of ASE along the film[25] and the generation of spectrally reproducible RL lines.[24] The spectral position of the relatively narrow, 10 meV, ASE line is located at 1.37–1.39 eV, as observed in Figure 1b, which is redshifted by 10–30 meV with respect to the PL peak energy at ≈1.395 eV (888 nm), and 60–90 meV below the energy band gap at 1.46 +/- 0.03 eV, as recently measured for these films by ellipsometry.[26]

The multilayer structure of the microcavity was designed to tune M0 within the PL energies. In particular, the bandpass of the DBRs was chosen to be centered at 880 nm with a full width at half maximum (FWHM) >80 nm, see Figure S1 (Supporting Information), the thicknesses of $FASnI_3$ (d_1) and Au (d_3) were fixed to d_1 = 200 nm and d_3 = 30 nm, respectively, while d_2, the PMMA thickness, was used as the tuning parameter for M0. Figure 1c plots the dispersion diagram of the device for d_2 = 250 nm calculated with a transfer matrix algorithm.[27] The structure presents the resonant mode M0 (green line) confined longitudinally in the cavity together with propagating modes in the Bragg mirror (black lines) and $FASnI_3$ film, G (brown line). Among these modes, the spontaneous emission (i.e., the PL) will be mainly coupled into M0 and G, because of the higher overlap of their power distribution with the active region. In particular, G is a guided mode that propagates the PL/ASE along the $FASnI_3$ plane with little influence on the thickness of the PMMA cladding, d_2.[28] At the same time, M0 is the resonance mode that outcouples the lasing emission in the vertical direction.[13] Accordingly, it is mandatory that the spectral position of M0 crosses the PL/ASE at 1.40 eV/1.37 eV, indicated as horizontal black lines in Figure 1c, in the angle of the collection system, gray area in Figure 1c. For this purpose, the thickness d_2 is the tuning parameter that shifts the M0 resonance energy, E_0, over the PL band.

The simulation of the reflectivity carried out by a transfer matrix method predicts the shift of the resonant wavelength(energy) $\lambda_0(E_0)$, between 800 nm (E_0 = 1.55 eV) and 910 nm (E_0 = 1.36 eV) for d_2 ranging between 100 and 260 nm, see Figure 1d. The predicted quality factor ($Q_0 = E_0/\Delta E$) for these optical modes would vary between 55 and 80. The same calculations indicate the power distribution of M0 mainly located at the PMMA/$FASnI_3$ films with a confinement factor (Γ) in the semiconductor Γ = 0.13, as shown in Figure 1e for d_2 = 250 nm (E_0 = 1.393 eV or λ_0 = 890 nm). According to the simulations, and following the procedure described in the methods section, twelve devices were fabricated in which the thickness of PMMA was slightly varied to shift the resonant energy, see Table S1 (Supporting Information). Figure S2 (Supporting Information) plots the experimental reflectivity in four representative samples where M0 is tunned from 800 (E_0 = 1.55 eV) and 910 nm (E_0 = 1.36 eV). It is worth mentioning that the Au film provided an excellent encapsulation for the $FASnI_3$ films preventing the degradation against air exposure that usually limits the performances of Sn-perovskites.[29] Indeed, all devices were measured at room temperature and ambient conditions without any additional encapsulation (or controlled inert atmosphere) usually needed in previous works to demonstrate ASE/lasing with Sn halide perovskites.[21,22,24,25,30] This improved stability is due to the use of several additives in the formulation of the molecular precursors for spin-coated $FASnI_3$ films used in the present work (see more details in Experimental Section), as previously demonstrated in Ref. 23. At these conditions, the devices operated over a whole working day (> 8 h) without appreciable degradation on their emission characteristics.

3. Mode Tuning throughout the PL Band

The initial strategy to control the emission properties of the RL is based on the spectral overlap of the resonant mode with emission/absorption energies. **Figure 2a** presents the evolution of the light emission spectra with the excitation fluence (P = 1–1500 μJ cm^{-2}) in five representative samples of the whole set, where M_0 is centered at E_0 = 1.54, E_0 = 1.49, E_0 = 1.44, E_0 = 1.40, and E_0 = 1.36 eV. Below the threshold of stimulated emission (P_{th}), the DBR-based cavity filters the spontaneous emission, leading to a structured PL spectrum in which an emission enhancement is observed around the spectral position of M0 (E_0); accordingly, the intensity of M0 increases linearly with the pump fluence, i.e., $I \propto P$, as observed in Figure 2c. Besides, above the threshold of stimulated emission, P_{th}, a narrower line centered 10–30 meV below the PL peak energy starts growing in intensity with a behavior that strongly depends on the resonant mode position. For E_0 = 1.54 eV, i.e., well above the absorption band edge, this emission line becomes dominant exhibiting a superlinear dependence with P, $I \propto P^a$ (a > 1), as observed in Figure 2c, and a progressive narrowing from 100 to 10 meV, Figure 2d, which is attributed to the generation of ASE mostly waveguided in the plane of the $FASnI_3$ thin film. This light is partially outcoupled at the surface of the device (in the vertical direction) by the tail of M0 overlapping the ASE line. In the case of E_0 = 1.49, 1.44 and 1.36 eV a set of narrow lines (3-5 meV) are superimposed to the background of the ASE band. These dominant lines are attributed to RL caused by the light waveguided along the $FASnI_3$ and scattered at its polycrystalline grains, as previously observed elsewhere.[24,30] Nevertheless, compared with these previous publications, the random resonant loops measured here are characterized by the following important and distinctive features: (i) RL lines appear immediately above threshold with small contribution of ASE (RL/ASE ratio>5-10), (ii) a reduced number of RL lines and even single-mode operation is observed for E_0 = 1.49 and 1.44 eV (around the bandgap of the $FASnI_3$), (iii) the lines are stable with the excitation laser fluence, see PL in linear scale in

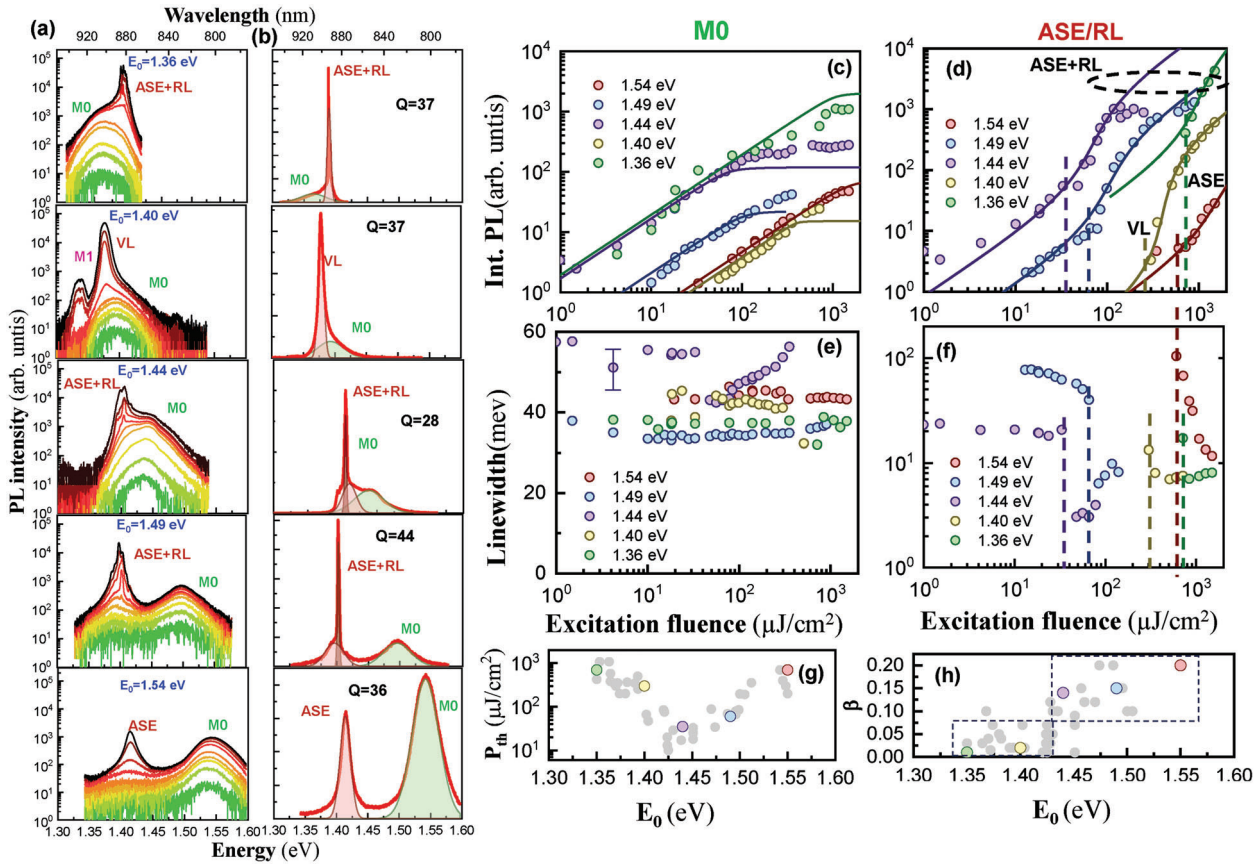

Figure 2. Dependence of the ASE/VL and the M0 bands with five representative positions of the resonant mode, E_0 = 1.55, red; 1.50, blue; 1.44, purple; 1.40, yellow; 1.36 eV, green. a) Spectra in log scale for excitations between 1 μJ cm^{-2} and 2 mJ cm^{-2}. b) Spectra in linear scale at P≈1.5P_{th} (red line) fitted with the sum of two gaussians distributions. Green and red areas represent the M0 and ASE/RL bands, respectively. Log-log plot of integrated intensity of the M0 (c), ASE/VL (d) bands as a function of the excitation fluence. Symbols and solid lines correspond to the experimental data and the fitting, respectively. Log-log plot of the linewidth of the M0 (e), ASE/VL (f) bands as a function of the excitation fluence. Dash line indicates P_{th}. g) P_{th} as a function of E_0 measured all samples (gray circles) h) β parameter deduced in all samples (gray circles). Color symbols in Figures (g) and (h) indicate the values of P_{th} and β obtained from the data depicted in Figures c-f.

Figure S3 (Supporting Information), (iv) the number of RL lines increases and the spectrum broadens by increasing the excitation fluence, in agreement with other RL devices.[16]

It is worth mentioning that we discard the observed narrow lines for E_0 = 1.36, 1.44, and 1.49 eV could be due to other resonant modes of the microcavity, because their linewidths are much narrower than that expected from the cavity Q-factor (Figure 1d), and hence unambiguously due to RL. These lines are observed at different energies over the ASE line, but not at the energies of the cavity mode (different by changing PMMA thickness). The last illustrated case corresponds to E_0 = 1.40 eV, where the microcavity is a Fabry-Perot with a resonance at the PL peak energy. Now, the spectra above P_{th} collapses into a lasing line, slightly narrower (7–8 meV) than the waveguided ASE observed in the case of E_0 = 1.55 eV, see Figure 2b, and maintains an almost constant shape with P, see Figure S3 (Supporting Information); the vertical lasing (VL) linewidth (Q ≈ 200) is limited by the low Q-factor of our microcavity at room temperature (Q_0 < 70). Indeed, similar DBR-metal cavities containing perovskite materials were producing lasing, but it was demonstrated only at cryogenic temperature[31] or with a much higher Q factor (≈1000) cavities.[32] Finally, in this sample, a replica of the lasing line located at lower energies, 1.32–1.33 eV is observed and labelled as M1, Figure 2a. The intensity of this third band is always >2 fold smaller than the main lasing line and it is ascribed to the coupling of the PL with a Bragg or cladding mode of the cavity, M1.

Following the plots presented in Figure 2a, the resonant cavity mode energy, E_0, produces a clear impact on the intensities of the observed lasing lines, their linewidth and P_{th}. The evolution of all contributions with P (PL, M0, and ASE/VL/RL) is determined by fitting the experimental spectra with the sum of two Gaussian shapes, as shown in Figure 2b; a third Gaussian function was only necessary to reproduce the ASE contribution for E_0 = 1.40 eV and E_0 = 1.44 eV in the range P = [0.5·P_{th},2·P_{th}]. From these fittings, the integrated intensity and linewidth of each gaussian contribution are plotted as a function of P in Figures 2c,d,e,f, respectively. In all samples, the M0 band grows linearly with P until saturation for P>P_{th}, see Figure 2c, while the lasing lines follow a S-curve (linear-superlinear-linear I-P dependence),[33] see Figure 2d. The linewidth of M0 change from sample to sample, but any variation is observed with P in most cases (fluctuations are observed in the sample with M0 at 1.44 eV, which is attributed

to its greater linewidth and the consequent greater error in the fitting), as shown in Figure 2e. Contrarily, from spontaneous emission to lasing regime an abrupt decrease in the spectrum linewidth is observed down to 3–8 meV, depending on the studied cases, which is characteristic of the optical gain generation (Figure 2f).[34]

More interestingly, the values of P_{th} deduced from Figure 2d–f are in the range of 35–700 μJ cm^{-2}, see dashed lines, suggesting an optimum E_0 in the range 1.42–1.45 eV, where RL or VL is enhanced. Besides, for E_0 = 1.40 eV, the mode is perfectly overlapped with the PL maximum and hence the cavity is presenting the maximum Purcell effect,[35–37] as shown in Figure S5 (Supporting Information) (continuous line), which is the reason of the observation of monomode VL (Figure 2a,b) with a linewidth limited by the cavity Q-factor. Counterintuitively, in microcavities with E_0 in the energy range 1.35–1.37 eV (see the statistics plotted in Figure 2g), RL lines are also observed, but P_{th} lies in the range 100–200 μJ cm^{-2}, higher than minimum values of P_{th} = 10–40 μJ cm^{-2} for the case of microcavities with resonant modes at E_0 = 1.42–1.45 eV. In both cases, RL lines are vertically outcoupled, which is attributed to the overlapping of M0 with the absorption band edge (X) instead of the PL maximum, where the semiconductor would be presenting a maximum of absorption/optical gain[34] without noticeable reabsorption of emitted light. Here, emitted light coupled to M0 experiences an important enhancement, as estimated experimentally in Figure S5 (Supporting Information). This minimum P_{th} = 10–40 μJ cm^{-2} is lower, but not far, than values reported in literature for multimodal RL measured in lead halide perovskites integrated in vertical microcavities.[14,15,38]

The experimental data shown in Figure 2c,d can be nicely reproduced, see solid lines, with standard laser equations considering two modes (the vertical cavity mode, M0, and the waveguided ASE/RL mode, G) for emitted photons, see Section S4 (Supporting Information). The spontaneous emission coupling factor, β, and the optical gain are output parameters can be extracted from this model. The statistics carried out in all samples (Figure 2h) indicate that $\beta > 0.1$ for E_0>1.42 eV, clearly above the values found for E_0<1.42 eV. The observed dependence of β on E_0 can be explained with the increasing absorption coefficient, and hence gain, within the energy range between the PL peak and the energy bandgap (slightly above due to the high inhomogeneity of the $FASnI_3$ film). Higher β values are also related to a stronger Purcell factor.[39] The optical gain in the system defines the carrier concentration at each excitation fluence, see Figure S4a (Supporting Information), that saturates in all samples to ≈600 cm^{-1} for the highest excitation, when stimulated emission and RL are taking place, see Figure S4b (Supporting Information). The gain value obtained here is lower than that deduced for planar waveguides containing the same active material, 1600 cm^{-1},[25] which is explained by the smaller confinement factor in the longitudinal/vertical mode (Γ = 0.13).

4. Spectral Position of RL

The spectral position of M0 not only presents an impact on the threshold and lasing parameters, but also on RL energy and its linewidth. The plot of the spectral energy of the vertically outcoupled ASE/VL and the RL lines measured in all samples as a function of E_0, **Figure 3a**, shows three distinguishable regions. First, ASE is observed in practically all samples with little influence on E_0 or if the device presents RL or not, see red rectangle. Indeed, the statistics, see Figure 3b, indicates that the ASE band is always centered at 1.375–1.390 eV, in agreement with our previous results for the Sn-perovskite in backscattering geometry and planar waveguides.[24,25] On the contrary, the generation of RL occurs at two spectral windows depicted with brown and blue rectangles in Figure 3a. Interestingly, the horizontal and vertical limits are different: (i) E_0 = 1.41–1.51 eV (above the PL peak energy and where the absorption band-edge is evident, see Figure 1b) promotes RL in the region 1.40–1.41 eV (region RL1), i.e., slightly above the PL peak energy; (ii) E_0 = 1.35–1.37 eV (low energy tail of the PL) that results in RL lines at 1.385–1.395 eV (region RL2), just very close to the PL peak energy. Moreover, we find two spectral regions for M0, E_0 = 1.38–1.42 eV and E_0>1.50 eV, where RL is not observed at all, which are ascribed to pure VL of the cavity and waveguided ASE.

At this point, it is necessary to elucidate what are the physical reasons for the dependence of the observed lasing structure on E_0. In a standard RL system, i.e., a film containing scattering centers, the RL is usually manifested as a multifrequency spectrum with very narrow lines superimposed to the background of the ASE line.[24,40,41] Contrarily, the light confinement and feedback provided by a cavity can enhance and privilege RL frequencies in the vertically outcoupled spectrum[13] or even inhibit the formation of RL in favor of the fundamental mode of the resonator.[38] In fact, emitted light by the $FASnI_3$ film integrated in the fabricated vertical cavity, can be coupled to the guided mode, responsible of the formation of RL lines,[25] and the resonant mode M0, responsible of the vertical emission,[31] as depicted in Figure 1c. The dominant mechanism will be determined by the balance between gain and loss for these two modes.[38] This will be the core hypothesis to understand and explain the results obtained by tuning M0, as discussed below.

Here, it is interesting to calculate the overlap of M0 with the PL/ASE band (Γ_{M0}), see Figure 3c. The maximum Γ_{M0} = 50–60% occurs in the spectral region where M0 is tuned around the PL peak, E_0 = 1.37–1.42 eV (indicated by the semitransparent green vertical frame in Figure 3a). This energy range for M0 coincides with the maximum of the spontaneous emission intensity and Purcell factor (Figure S5, Supporting Information) of the $FASnI_3$ film, where also the semiconductor experiences sufficient gain and low reabsorption losses, promoting an optimum and dominant coupling to M0. This coupling gives rise to the vertical cavity lasing characteristic of planar microcavities.[42] When E_0 = 1.42–1.50 eV, the wide linewidth of M0 still overlaps the high-energy side of the PL band (Γ_{M0} = 20-30%), resulting on an efficient coupling with the guiding mode that promotes RL1 along the $FASnI_3$ plane, see the illustration in the top panel Figure 3d. Consequently, RL lines generated in this second region will be outcoupled in the vertical direction through M0. Similarly occur in third spectral region, E_0 = 1.35–1.38 eV, within the low-energy side of the PL spectrum. Again, the overlap of M0 with the PL, ΓM0 = 30–40%, is high enough dominant to outcouple vertically the RL2 lines generated in the semiconductor film, see the illustration at the bottom panel of Figure 3d. Interestingly, 3–4 lasing lines are observed for RL2, whereas only 1–2 lines in the case of RL1, as depicted in Figure 3e (the central green shadowed

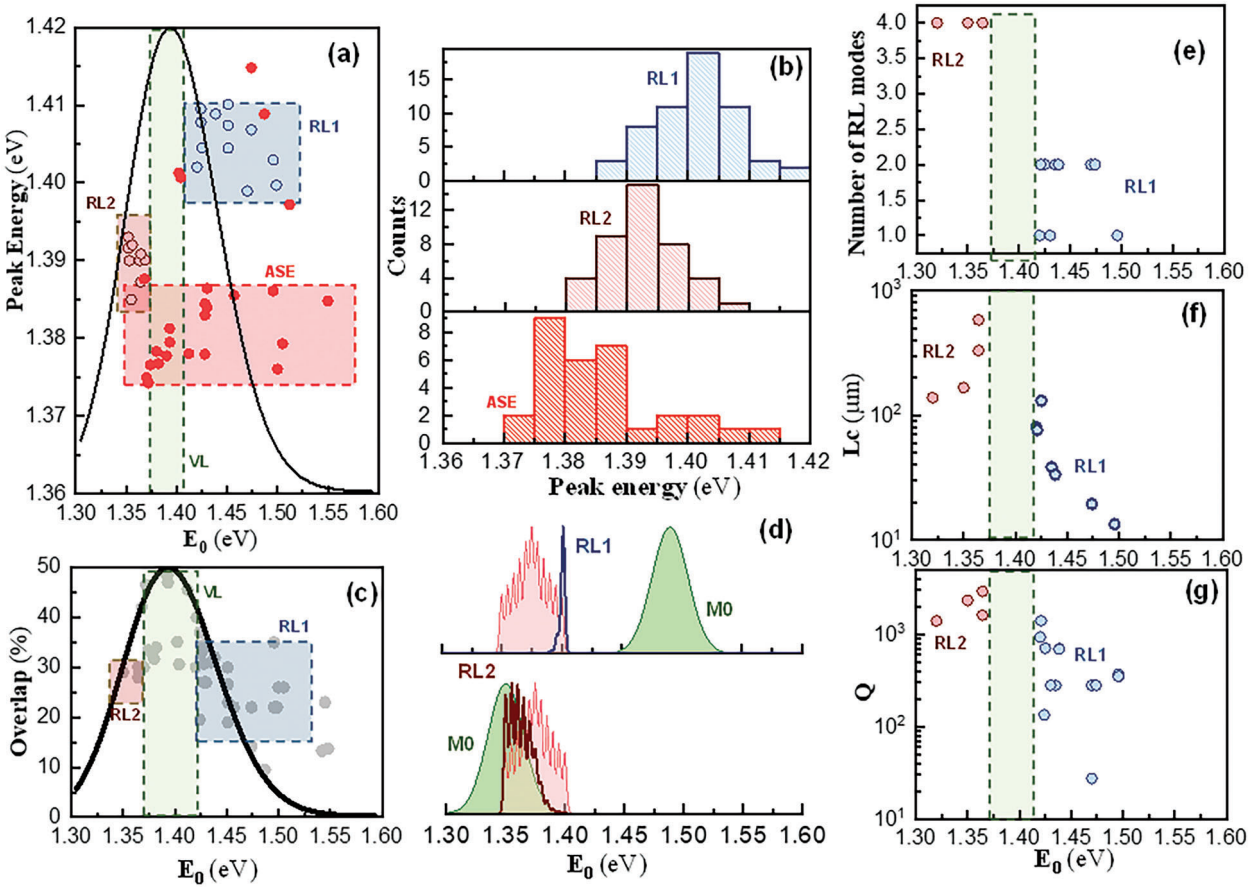

Figure 3. Statistics of ASE, vertical lasing and RL. a) Energy of ASE/lasing (red symbols) and RL (brown symbols) as a function of the mode position plotted together with the PL spectrum (black solid line). The graphic indicates three different regions for ASE (red frame), VL (green frame) RL1 (blue frame) and RL2 (brown frame). b) Statistics of emission of ASE/VL, RL1, RL2. c) Overlap of M0 (gray symbols) with the PL (black line). d) Emission spectra resulting from the convolution of M0 (green area) with the modulated ASE line (red area) for $E_0 = 1.49$ eV and $E_0 = 1.36$ eV. Number of RL (e), cavity length (f), and Q-factor (g) as a function of E_0. The green frame indicates the VL region.

rectangle is the same used in Figure 3b indicating the M0-promoted vertical lasing). The biggest difference between RL2 and RL1 is the much lower absorption coefficient in the first case, a situation that can promote differences in gain (photogenerated carrier density), larger propagation distances through the guided mode and longer RL loops, as discussed below, as compared with the case of RL1, which is characterized by near single lasing modes and shorter RL loops; moreover, the minimum lasing threshold was observed for RL1.

The losses in a RL system comprises the absorption in the film and the scattering in the random loop.[1] Furthermore, the gain and absorption loss are increasing with energy above the absorption band edge of the semiconductor. The RL loop length is determined by the average distance between consecutive scatters.[1] A fast Fourier transform made for the different spectra yields the size of effective cavity (L_C) formed by the scattering loops.[43] We observe that L_C depends on the spectral region where the RL is formed, see Figure 3f. In the RL2 region, even if the gain is very low, the absence of self-absorption losses promotes the narrowest RL lines at 1.385–1.395 eV with the longest loops, L_c = 100–1000 μm, containing typically four RL frequencies. In contrast, in the RL1 region, 1.40–1.41 eV is the preferable emission window, where gain increases. Consequently, the RL loops are concentrated into smaller sizes, L_c<100 μm, leading to 1–2 RL modes. Indeed, in cavities with M0 tuned to the highest mode energies, the RL emission is extremely localized, L_c ≈10 μm, see Figure S6 (Supporting Information) for an image of these loops, resulting in near single-mode RL operation with excellent stability in time and excitation fluence, see Figure S7 (Supporting Information) and next section. Simultaneously, the higher self-absorption losses that generate the shorter RL1 loops above 1.42 eV, is accompanied by an increase of RL1 linewidths, hence decreasing the lasing Q-factor below 1000 (blue circles in Figure 3g). In the RL2 region Q values appear in the range 1000–3000 (red circles in Figure 3g), which are similar to values previously measured in backscattering geometry (18), but RL2 lines exhibited lasing thresholds more than one order of magnitude higher than in the case of RL1 ones.

5. Tuning/Tailoring RL Properties

According to the previous discussion, the spectral position of the resonant mode of the Fabry-Perot cavity, E_0, can be used to tailor the number of RL modes, to reduce the threshold and increase

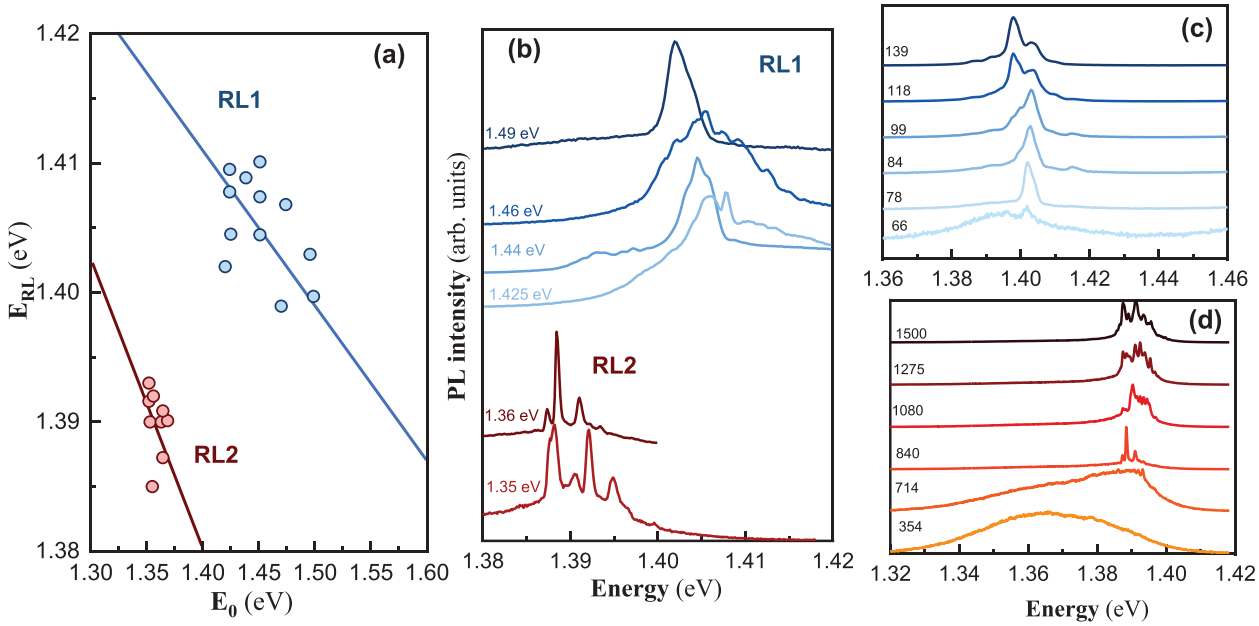

Figure 4. Tailoring of RL properties. a) Shift of RL energy and mode energies as a function of E_0. b) RL spectra obtained at different mode Energies E_0 = 1.49, 1.46, 1.44, 1.425, 1.36 and 1.35 eV. Evolution of the RL with the excitation fluence: c) E_0 = 1.49 eV, d) E_0 = 1.36 eV.

the Q value of the lasing mode, and, more interestingly, determining the position of RL lines over two well defined emission windows, 1.40–1.41 eV (E_{RL1}) and 1.385–1.395 eV (E_{RL2}), approximately, as observed in Figures 3a and 4a, which is determined by E_0. Within the dispersion of the data, the shift of E_{RL} versus E_0 suggests nearly linear dependences with E_0, E_{RL1} = 1.405–0.14·(E_0-E_{PL}) and E_{RL2} = 1.388–0.08·(E_0-E_{PL}) in the regions RL1 and RL2, respectively, as shown in **Figure** 4a. Correspondingly, the variation of E_0 above/below the center of the PL band, E_{PL} = 1.395 eV, yields a RL1/RL2 energy slightly above/below E_{PL}.

Figure 4b shows the RL spectra of six points with different E_0 following the law obtained in Figure 4a. Although it is necessary to carry out additional investigations to explain this behavior, we believe that the overlap of the M0 with PL energy states and the variation of gain with energy play an important role in the tuning of E_{RL}. In both regions the overlap decreases with the absolute shift $\Delta = |E_0\text{-}1.40|$. However, the system presents a smaller effective gain for RL2, contrary to the case of RL1 where gain increases, leading to a reduced number of small loops. At these conditions, for the highest Δ the system becomes single-mode in return to higher thresholds and lower lasing Q-factor due to the higher re-absorption losses. Figure 4c,d plot the RL evolution with the excitation fluences for E_0 = 1.49 eV (Figure 4c) and E_0 = 1.36 eV (Figure 4d), respectively. Clearly, the RL2 becomes multimode with the excitation fluence, whereas the single mode RL1 is stable with the excitation fluence, as observed in Figure 4c and Figure S7 (Supporting Information).

6. Lasing in Inkjet-Printed Films

To test the scalability of our laser device, 2D/3D $(PEA_{0.5},BA_{0.5})_2FA_9Sn_{10}I_{31}$ thin films were prepared by inkjet printing using the appropriate precursors in DMF/DMSO solvents (9:1) and stirred at room temperature. The best ink printability was reached by adding 0.016 M of SnF_2 and 1 mM of $NaBH_4$ to the precursor solution, which improves the stability of the film against oxidation.[23,44] The 2D/3D phase is used to properly crystalize the film during inkjet printing, and also influence positively the stability of the device. The ink ejection frequency of 2.0 kHz and a resolution of 560 drops per inch (DPI) was used. The Sn-perovskite film presents a greater thickness inhomogeneity as compared to the spincoated samples, but lasing is easily found over the whole sample surface of a DBR-based microcavity integrating this film and the PMMA/gold cladding and top mirror.

The device exhibits RL operation with similar characteristics as its counterpart fabricated by spin coating, see **Figure** 5a. The cavity was designed with a mode at around E_0 = 1.42 eV in order to obtain RL1-type RL at 1.419 eV, see Figure 5b, above a threshold of ≈100 μJ cm^{-2}, see Figure 5c, and a linewidth of 5 meV (see Figure 5d) at the highest available excitation fluence.

This is another important result toward the development of RL devices based on 2D/3D Sn perovskites by inkjet printing technology, which, to the best of our knowledge, is the first experimental demonstration of lasing, as a starting point for the future development of microlasers fabricated with this proved technology.

7. Conclusion

In this manuscript, we successfully demonstrated the precise manipulation of the RL properties in Pb-free perovskite $FASnI_3$ thin films through the utilization of an economical and scalable low-Q vertical cavity architecture. For this purpose, the sweep of the energetic position of the longitudinal mode of the cavity across the semiconductor's PL/bandgap energy allowed the control of the RL threshold, emission energy, linewidth, and the number of RL modes emitted by the perovskite material. Optimal RL

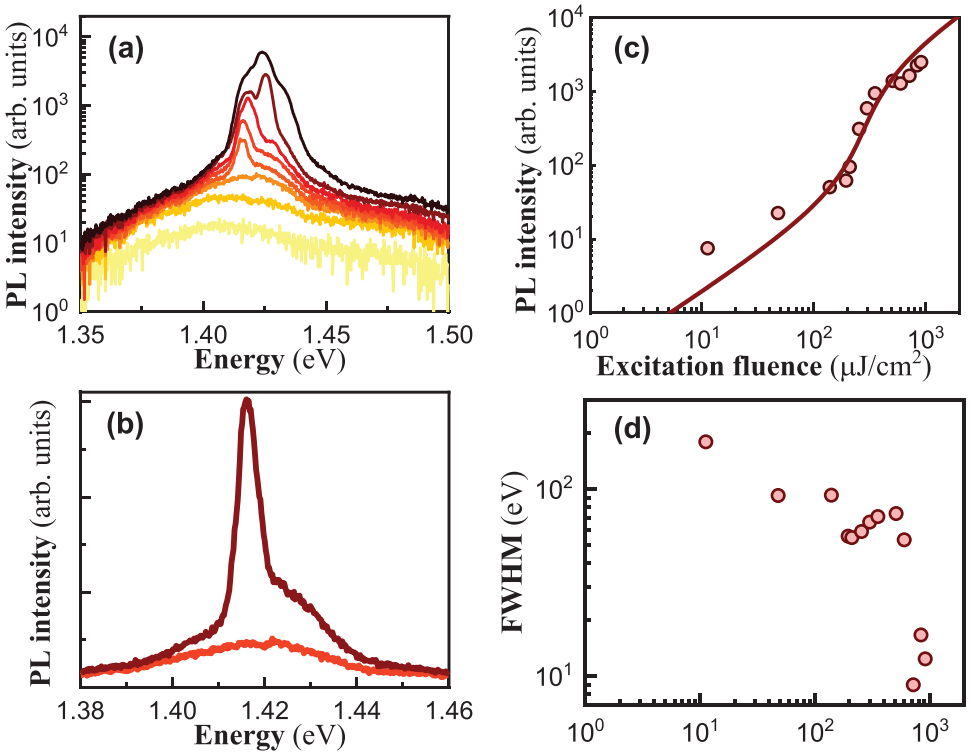

Figure 5. RL with a $FASnI_3$ film fabricated by ink-jet printing. a) Emission spectra at different excitation fluences. b) Emission spectra below and above threshold. c) Log-log plot of the PL intensity as a function of the excitation fluence. d) Log-log plot of the linewidth as a function of the excitation fluence.

emission in the vertical direction is attained when the mode is either blue or redshifted over the PL peak energy, creating two distinct spectral regions (defined by lower/higher gain) with unique and stable emission profiles. Notably, for certain mode positions the cavity shows monochromatic RL emission at room temperature, which, as far as we know, is the first time where it is obtained for the Sn-perovskite. Moreover, the fabrication of the device can be extrapolated from spin-coating to a scalable inkjet printing technology, thus, opening the doors to the possibility of industrial-scale production. This straightforward and versatile approach paves the way for tailored RL characteristics, with potential applications in the implementation of cheap and adaptable optical sources. Furthermore, typical vertical cavity lasing was also demonstrated when M0 is tuned to the PL maximum energy (maximum overlap), where the balance between gain and losses is positive and the Purcell factor is maximum; in this way, high-Q quality cavities can be also developed in the future for standard vertically emitting lasers.

8. Experimental Section

Tin (II) iodide (SnI_2, 99.99%), tin(II) fluoride (SnF_2, 99%), N,N-dimethylformamide (DMF, 99.8%) and dimethylsulfoxide (DMSO, 99.8%) were purchased from Sigma-Aldrich. Formamidinium iodide (FAI. 99.99%) was purchased from Greatcell Solar Materials. These materials were used as received with no further purifications.

Dipropylammonium iodide salt was synthesized with the following procedure: 10 g Dipropylamine was added to 30 mL of cold EtOH. Then 13 mL of HI was added dropwise to the flask under vigorous stirring. The white solid formed after the addition of HI was filtered and washed with 100 mL of cold diethylether and it was recrystallized using EtOH.

To prepare the $FASnI_3$ precursor solution, 298 mg of SnI_2 (0.8 M), 123.8 mg of FAI (0.72 M), 36.65 mg of DipI (0.16 M), 0.1 mg of sodium borohydride, $NaBH_4$, (0.0026 M, this value might vary depending on the batch and purity of the precursor) and 12.48 mg of SnF_2 (0.08 M) were dissolved in 1 mL of a mix solution of DMSO:DMF (9:1, v/v) and stirred over night at room temperature. The combination of $NaBH_4$ and DipI additives produced a synergistic effect in $FASnI_3$ films increasing their stability, where the former was a reducing agent avoiding Sn^{+2} oxidation while the latter acted as a passivating agent, resulting in an enhancement of their optoelectronic properties under N_2 and ambient conditions, as discussed in previous works.[23,26]

The commercial DBR mirrors (central wavelength 890 nm, supplied by Edmund Optics, Ref. 63 154, and Eksma Optics, Ref. 031-0890-i0) were polished from the back-side for light transmission proposals. Then, the mirrors were washed with ethanol, acetone and isopropanol, respectively in an ultrasonic bath for 5 min each. After the wash, the substrates were dried with N_2 flux, and right before the perovskite film, they were treated in UV-Ozone for 10 min. The perovskite film was deposited by one step antisolvent method, by adding $FASnI_3$ precursor solution (with the additives indicated above: DipI and $NaBH_4$) inside a N_2-filled glovebox, on top of the appropriate substrates and spin coated at 4000 rpm for 50 s. Then 400 μL of Chlorobenzene was drop on top of the substrate after 20 s of spinning, followed by an annealing at 70 and 100 °C for 1 min and 19 min, respectively.

$(PEA_{0.5},BA_{0.5})_2FA_9Sn_{10}I_{31}$ thin films were prepared by inkjet printing. The ink was planned based on mixing DMF/DMSO solvents (9:1) and stirred at room temperature. The best ink printability was reached by adding 0.016 M of SnF_2 and 1 mM of $NaBH_4$ to the precursor solution. An ink ejection frequency of 2.0 kHz and a resolution of 560 drops per inch (DPI) was used. During the printing onto the DBR-structure-on-glass substrate, the platen substrate temperature was kept constant below

<20 C (chiller maintaining the temperature control inside the glovebox) in order to promote a proper spreading and adhesion among the different sublayers piled up to complete the thick full layer. The filtered solution of the perovskite ink, with a viscosity ≈2 cP, was printed with a fixed drop-volume of 10 pL through 21-µm diameter nozzle by using the cartridge for Dimatix printers (Fujifilm Dimatix Inc.). To control the crystallization growth, ensuring low nucleation point and big grain without defects, after the inkjet-printing process, the layers were submitted to the curing process based on N_2 air flow at 1 bar pressure (from 5 cm distance) onto the hot-plate annealing at 85 C for 10 min. Then finally a final vacuum annealing was completed for 10 min at 60 C.

Once the perovskite thin films were deposited on the mirror, a PMMA solution (100 mg/1 mL CB) was spin coated on top of the perovskite film for 30 s and annealed at 70 °C for 1 min and 4 min at 100 °C. The speed was ranged between 1000 and 4000 rpm to tune the thickness. The device was completed by evaporating a 30 nm Au film on the top of the PMMA.

Reflectivity of the whole devices was measured by using a commercial reflectometer (NanoCalc 2000 from Micropak).

To characterize the lasers, the devices were pumped at 532 nm pulsed laser (1 ns, 100 Hz–20 kHz) from the back side of the mirrors with a 20x microscope objective. The excitation fluence was controlled with neutral density filters. The size of the excitation spot was optimized for the maximum RL/ASe signal (≈0.2 mm^2). The emitted PL was collected from the top Au with another 20x microscope objective, dispersed by a grating spectrograph (DNS-300 from DeltaNu) and detected by a back-illuminated Si CCD (DV420A-OE from Andor) at its exit.

Supporting Information

Supporting Information is available from the Wiley Online Library or from the author.

Acknowledgements

This project received funding from the European Union's Horizon 2020 research and innovation programme under grant agreement No 862656 (project DROP-IT), by the Spanish MINECO through projects no. PID2020-120484RB-I00, PID2022-140090OB-C21 (PLEDs project) and PID2022-140978OB-I00. This study also forms part of the Advanced Materials (project no. MFA/2022/020) and Quantum Communication programmes (project no. COMCUANTICA/009) and was supported by MCIN with funding from European Union NextGenerationEU (PRT-RC17.11) and by Generalitat Valenciana. H. P. A also acknowledges the support from the European Union's Horizon 2020 (project DROP-IT, No 862656) and Generalitat Valenciana's PROMETEO program (project PROMETEU/2021/082).

Conflict of Interest

The authors declare no conflict of interest.

Data Availability Statement

The data that support the findings of this study are available from the corresponding author upon reasonable request.

Keywords

amplified spontaneous emission, $FASnI_3$, lead free perovskite, random lasing, vertical cavity laser

Received: December 6, 2023
Revised: March 4, 2024
Published online:

[1] R. Sapienza, *Nat. Rev. Phys.* **2019**, *1*, 690.
[2] D. S. Wiersma, *Nat. Phys.* **2008**, *4*, 359.
[3] F. Luan, B. Gu, A. S. L. Gomes, K.-T. Yong, S. Wen, P. N. Prasad, *Nano Today* **2015**, *10*, 168.
[4] S. Lepri, S. Cavalieri, G. L. Oppo, D. S. Wiersma, *Phys. Rev. A* **2007**, *75*, 063820.
[5] N. Bachelard, S. Gigan, X. Noblin, P. Sebbah, *Nat. Phys.* **2014**, *10*, 426.
[6] N. Caselli, A. Consoli, Á. M. Mateos Sánchez, C. López, *Optica* **2021**, *8*, 193.
[7] Q. Song, S. Xiao, X. Zhou, L. Liu, L. Xu, Y. Wu, Z. Wang, *Opt. Lett.* **2007**, *32*, 373.
[8] M. Rashidi, T. Haggren, C. Jagadish, H. H. Tan, *ACS Photonics* **2022**, *9*, 3573.
[9] T. Zhai, J. Chen, L. Chen, J. Wang, L. Wang, D. Liu, S. Li, H. Liu, X. Zhang, *Nanoscale* **2015**, *7*, 2235.
[10] L. Ye, F. Li, C. Lu, Z. Cheng, G. Hu, Y. Lu, Y. Cui, *Nanophotonics* **2018**, *7*, 473.
[11] J. Zhang, F. Wang, S. Ghafoor, H. Wang, W. Zhang, K. Xie, R. Cheng, J. Yan, L. Niu, P. Wang, L. Zhang, Z. Hu, *Adv. Opt. Mater.* **2022**, *10*, 2200426.
[12] T. Zhai, X. Zhang, Z. Pang, X. Su, H. Liu, S. Feng, L. Wang, *Nano Lett.* **2011**, *11*, 4295.
[13] Q. Song, L. Liu, S. Xiao, X. Zhou, W. Wang, L. Xu, *Phys. Rev. Lett.* **2006**, *96*, 033902.
[14] P. Bouteyre, E. Deleporte, J.-S. Lauret, G. Trippé-Allard, G. Delport, F. Lédée, H. S. Nguyen, A. Belarouci, C. Seassal, D. Garrot, F. Bretenaker, H. Diab, *Opt. Express* **2020**, *28*, 39739.
[15] Y. Liu, W. Yang, S. Xiao, N. Zhang, Y. Fan, G. Qu, Q. Song, *ACS Nano* **2019**, *13*, 10653.
[16] J. Liu, P. D. Garcia, S. Ek, N. Gregersen, T. Suhr, M. Schubert, J. Mørk, S. Stobbe, P. Lodahl, *Nat. Nanotechnol.* **2014**, *9*, 285.
[17] M. Lee, S. Callard, C. Seassal, H. Jeon, *Nat. Photonics* **2019**, *13*, 445.
[18] L. N. Quan, B. P. Rand, R. H. Friend, S. G. Mhaisalkar, T. W. Lee, E. H. Sargent, *Chem. Rev.* **2019**, *119*, 7444.
[19] B. R. Sutherland, E. H. Sargent, *Nat. Photonics* **2016**, *10*, 295.
[20] W. F. Yang, F. Igbari, Y. H. Lou, Z. K. Wang, L. S. Liao, *Adv. Energy Mater.* **2020**, *10*, 1902584.
[21] R. L. Milot, G. E. Eperon, T. Green, H. J. Snaith, M. B. Johnston, L. M. Herz, *J. Phys. Chem. Lett.* **2016**, *7*, 4178.
[22] G. Xing, M. H. Kumar, W. K. Chong, X. Liu, Y. Cai, H. Ding, M. Asta, M. Grätzel, S. Mhaisalkar, N. Mathews, T. C. Sum, *Adv. Mater.* **2016**, *28*, 8191.
[23] J. Sanchez-Diaz, R. S. Sánchez, S. Masi, M. Krecmarová, A. O. Alvarez, E. M. Barea, J. Rodriguez-Romero, V. S. Chirvony, J. F. Sánchez-Royo, J. P. Martinez-Pastor, I. Mora-Seró, *Joule* **2022**, *6*, P861.
[24] V. S. Chirvony, I. Suárez, J. Sanchez-Diaz, R. S. Sánchez, J. Rodríguez-Romero, I. Mora-Seró, J. P. Martínez-Pastor, *Adv. Mater.* **2023**, *35*, 2208293.
[25] I. Suárez, V. S. Chirvony, J. Sánchez-Díaz, R. S. Sánchez, I. Mora-Seró, J. P. Martínez-Pastor, *Adv. Opt. Mater.* **2022**, *10*, 2200458.
[26] G. Mannino, J. Sanchez-Diaz, E. Smecca, S. Valastro, I. Deretzis, R. S. Sánchez, J. P. Martinez-Pastor, I. Mora-Seró, A. Alberti, *Sol. RRL* **2023**, *7*, 2300610.
[27] G. Lifante, *Integrated Photonics: Fundamentals*, J. Wiley, Hoboken, NJ **2002**.
[28] I. Suárez, E. J. Juárez-Pérez, V. S. Chirvony, I. Mora-Seró, J. P. Martínez-Pastor, *Phys. Rev. Appl.* **2020**, *13*, 064071.
[29] L. Lanzetta, T. Webb, N. Zibouche, X. Liang, D. Ding, G. Min, R. J. E. Westbrook, B. Gaggio, T. J. Macdonald, M. S. Islam, S. A. Haque, *Nat. Commun.* **2021**, *12*, 2853.
[30] Z. Y. Wu, Y. Y. Chen, L. J. Lin, H. C. Hsu, *J. Phys. Chem. C* **2021**, *125*, 5180.

[31] J. Wang, P. Da, Z. Zhang, S. Luo, L. Liao, Z. Sun, X. Shen, S. Wu, G. Zheng, Z. Chen, *Nanoscale* **2018**, *10*, 10371.
[32] S. Chen, A. Nurmikko, *ACS Photonics* **2017**, *4*, 2486.
[33] L. A. Coldren; S. W. Corzine; M. Masanovic, *Diode Lasers and Photonic Integrated Circuits*, Wiley, Hoboken, N.J **2012**.
[34] I. Suárez; J. P. Martínez-Pastor, *Halide Perovskites for Photonics. Chapter 7. Generation of Amplified Spontaneous Emission in Lead Halide Semiconductors*, edited by A. Vinattieri, G. Giorgi, AIP Publishing LLC, Melville, NY **2021**, pp. 1–40.
[35] T. Baba, T. Hamano, F. Koyama, K. Iga, *IEEE J. Quantum Electron.* **1992**, *28*, 1310.
[36] J. Wang, R. Cao, P. Da, Y. Wang, T. Hu, L. Wu, J. Lu, X. Shen, F. Xu, G. Zheng, Z. Chen, *Appl. Phys. Lett.* **2015**, *1*, 022103.
[37] A. Meldrum, P. Bianucci, F. Marsiglio, *Opt. Express* **2010**, *18*, 10230.
[38] I. Goldberg, N. Annavarapu, S. Leitner, K. Elkhouly, F. Han, N. Verellen, T. Kuna, W. Qiu, C. Rolin, J. Genoe, R. Gehlhaar, P. Heremans, *ACS Photonics* **2023**, *10*, 1591.
[39] J. B. Khurgin, M. A. Noginov, *Laser Photonics Rev.* **2021**, *15*, 2000250.
[40] J. Fallert, R. J. B. Dietz, J. Sartor, D. Schneider, C. Klingshirn, H. Kalt, *Nat. Photonics* **2009**, *3*, 279.
[41] R. C. Polson, M. E. Raikh, Z. V. Vardeny, *IEEE J. Sel. Top. Quantum Electron.* **2003**, *9*, 120.
[42] G. BjÖrk, Y. Yamamoto, *IEEE J. Quantum Electron.* **1991**, *27*, 2386.
[43] R. C. Polson, G. Levina, Z. V. Vardeny, *Appl. Phys. Lett.* **2000**, *76*, 3858.
[44] G. Vescio, J. Sanchez-Diaz, J. L. Frieiro, R. S. Sánchez, S. Hernández, A. Cirera, I. Mora-Seró, B. Garrido, *ACS Energy Lett.* **2022**, *7*, 3653.